

Plasmonic engineering of singlet oxygen generation

Yongxia Zhang, Kadir Aslan, Michael J. R. Previte, and Chris D. Geddes*

Institute of Fluorescence, Laboratory for Advanced Medical Plasmonics, and Laboratory for Advanced Fluorescence Spectroscopy, Medical Biotechnology Center, University of Maryland Biotechnology Institute, 725 West Lombard Street, Baltimore, MD 21201

Edited by Nicholas J. Turro, Columbia University, New York, NY, and approved December 18, 2007 (received for review October 5, 2007)

In this article, we report metal-enhanced singlet oxygen generation (ME^1O_2). We demonstrate a direct relationship between the singlet oxygen yield of a common photosensitizer (Rose Bengal) and the theoretical electric field enhancement or enhanced absorption of the photosensitizer in proximity to metallic nanoparticles. Using a series of photosensitizers, sandwiched between silver island films (SiFs), we report that the extent of singlet oxygen enhancement is inversely proportional to the free space singlet oxygen quantum yield. By modifying plasmon coupling parameters, such as nanoparticle size and shape, fluorophore/particle distance, and the excitation wavelength of the coupling photosensitizer, we can readily tune singlet oxygen yields for applications in singlet oxygen-based clinical therapy.

metal-enhanced fluorescence | metal-enhanced phosphorescence | photodynamic therapy | surface-enhanced fluorescence

Photodynamic therapy (PDT) has been widely used in both oncological (e.g., tumors and dysplasias) and nononcological (e.g., age-related macular degeneration, localized infection, and nonmalignant skin conditions) applications (1–4). Three primary components are involved in PDT: light, a photosensitizing drug, and oxygen. The photosensitizer adsorbs light energy, which it then transfers to molecular oxygen to create an activated form of oxygen called singlet oxygen (1O_2). The singlet oxygen is a cytotoxic agent and reacts rapidly with cellular components to cause damage that ultimately leads to cell death and tumor destruction (4). PDT treatments are only effective within a specific range of singlet oxygen supply (5). For example, for solid tumors, too little singlet oxygen cannot effectively treat the tumor cells, but too much singlet oxygen can damage and kill surrounding healthy cells (6). Currently, the intensity of light is commonly adjusted to control the extent of singlet oxygen generation, but there are some limitations to this method. High fluency rates of the exposure light will lead to oxygen depletion and photosensitizer photobleaching (3). However, low fluency rates of exposure light leads to a long exposure time and can cause vascular shutdown, a precursory condition to hypoxia in the tissue (5, 7). One notable approach to controlling the fluency rate of exposure light is called interstitial PDT, where a precise amount of light is delivered locally to tumors through inserted optical fibers (8). The interstitial PDT also allows the real-time monitoring of the progression of the treatment via online collection of assessment parameters through the optical fibers (8). It is important to note that despite the better control over fluency rate, the photobleaching of the photosensitizers remains an issue. In this regard, our laboratory has introduced a metal-enhanced phenomenon as a means to control the extent of singlet oxygen generation via metal–photosensitizer interactions, an alternative approach as compared with exposure settings and sensitizer dose, which we believe is a significant improvement for future PDT.

Our laboratories have for many years been investigating the near-field interactions of fluorophores with metallic nanoparticles, a phenomenon called metal-enhanced fluorescence (MEF) (9). According to our current interpretation of MEF (shown in Fig. 1A), nonradiative energy transfer occurs from excited distal fluorophores to the surface plasmon electrons on noncontinuous films (10). The surface plasmons in turn radiate

the photophysical characteristics of the coupling fluorophores. In addition to MEF, we have also reported metal-enhanced phosphorescence (MEP) at low temperature (11, 12), whereby nonradiative energy transfer is thought to occur from excited distal triplet-state luminophores to surface plasmons in noncontinuous silver films, which in turn radiate luminophore emission efficiently (Fig. 1B). Subsequently, we have observed an enhanced net system absorbance that contributes to the increase in singlet and triplet yields for Rose Bengal (RB) (11, 12).

In a previous rapid communication, we reported the observation of the ME^1O_2 phenomenon, where silver island films (SiFs) can enhance singlet oxygen generation (Fig. 1C) (13). We postulated that the enhanced singlet oxygen yields were a result of the increase in the net system absorbance or enhanced triplet yield. However, we did not present a method to optimize or control the amount of singlet oxygen generation from photosensitizers in proximity to metal nanoparticles, nor did we show the general applicability of the technology to a wide range of photosensitizers.

Because enhanced electromagnetic fields in proximity to metal nanoparticles are the basis for the increased system absorption, various computational methods are available to predict the extent of the net system absorption and potentially model the relative increase in singlet oxygen generation from photosensitizers (14–16). In comparison with traditional Mie theory, more accurate computational methods, such as discrete dipole approximation (DDA) (17) or finite difference time domain (FDTD) (16, 18, 19), are often implemented to more accurately approximate field distributions for larger particles with quadruple plasmon resonances, plasmon frequencies of silver nanoparticles, or nonspherical nanoparticles in complex media or arrangements (17, 18, 20, 21).

In this article, we use FDTD methods to demonstrate direct evidence for the relationship of electric field enhancements around nanoparticles and the increase in triplet yields for a photosensitizer and the subsequent increase in singlet oxygen generation. We have studied several photosensitizers with singlet oxygen yields ranging from 0.08 to 1.00 sandwiched between SiFs for metal-enhanced singlet oxygen generation (ME^1O_2). We observed an inverse relationship between the singlet oxygen enhancement factor and the free-space singlet oxygen quantum yield. In addition, we observed a distance dependence for the generation of ME^1O_2 from photosensitizers on SiFs substrates by using SiO_x layers 0.5, 2, 5, and 10 nm thick. These observations are consistent with numerous distance dependence measurements for MEF and MEP themselves. This observation of metal-enhanced 1O_2 generation is not only helpful in furthering our understanding of plasmon–luminophore interactions but also suggests that this approach may be an alternative method for controlling the generation of singlet oxygen for PDT, where an optimized amount of 1O_2 is required.

Author contributions: C.D.G. designed research; Y.Z. performed research; K.A. and M.J.R.P. analyzed data; and Y.Z. wrote the paper.

The authors declare no conflict of interest.

This article is a PNAS Direct Submission.

*To whom correspondence should be addressed. E-mail: geddes@umbi.umd.edu.

© 2008 by The National Academy of Sciences of the USA

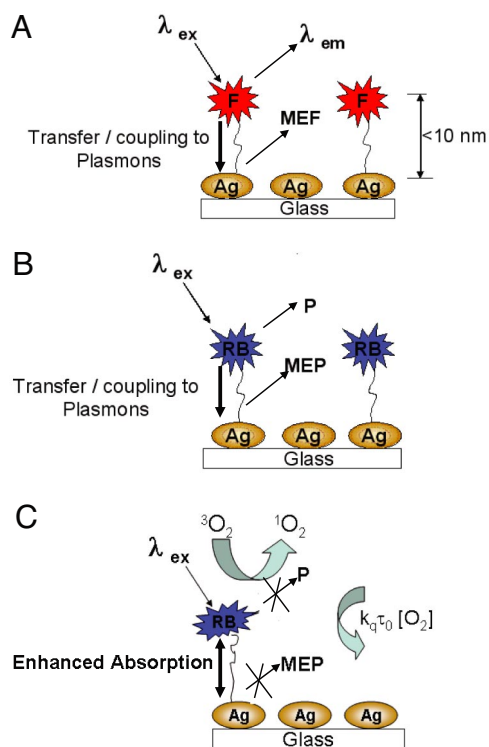


Fig. 1. Interpretation of MEF. Shown are graphical representations of MEF (A), metal-enhanced phosphorescence (B), and the generation of singlet oxygen (C). F, fluorophore; P, phosphorescence; $^3\text{O}_2$, triplet ground state oxygen; $^1\text{O}_2$, singlet oxygen.

Results and Discussions

Because RB is a commonly used photosensitizer with high singlet oxygen yield (0.76), it was selected to demonstrate the properties of metal-enhanced singlet oxygen generation (22). We note that although several singlet oxygen detection reagents are available (23, 24), our choice of singlet oxygen sensor green reagent (GR) lies in the fact that it is highly selective for singlet oxygen (24) and thus is highly suitable for the work undertaken here. The solutions of GR and RB have well separated fluorescence peaks at 525 nm (Fig. 2A) and 588 nm (Fig. 2B). The green sensor detects singlet oxygen (24), whereas RB is the photosensitizer that triggers singlet oxygen generation through a triplet interaction with ground-state molecular oxygen. Without UV irradiation (sensitization), we observed a green fluorescence emission peak at 525 nm for the GR singlet oxygen sensor on glass (Fig. 2A). We attribute this result to background solution singlet oxygen and emission of the sensor dye (25). Because of the MEF effect (9), the fluorescence emission peak of GR is enhanced on SiFs (Fig. 2A), which we correct for in our calculation of enhanced singlet oxygen yields (MEF factor; Eq. 1). As we previously reported, we also observe a MEF effect in the RB spectra for the sample on SiFs (Fig. 2B) (12).

After exposure to UV light, the fluorescence emission intensity of GR on SiFs (Fig. 2D) at 525 nm is ≈ 3.3 times larger than GR emission on glass (Fig. 2C). This increased intensity suggests that more singlet oxygen was generated from the RB system on SiFs. The real-color photographs further validated the difference of GR fluorescence emission intensity on glass and SiFs, respectively (Fig. 2C and D, *Insets*). On glass, real-color photographs of GR/RB solutions (Fig. 2C *Insets*) before exposure to UV light are visually brighter after expo-

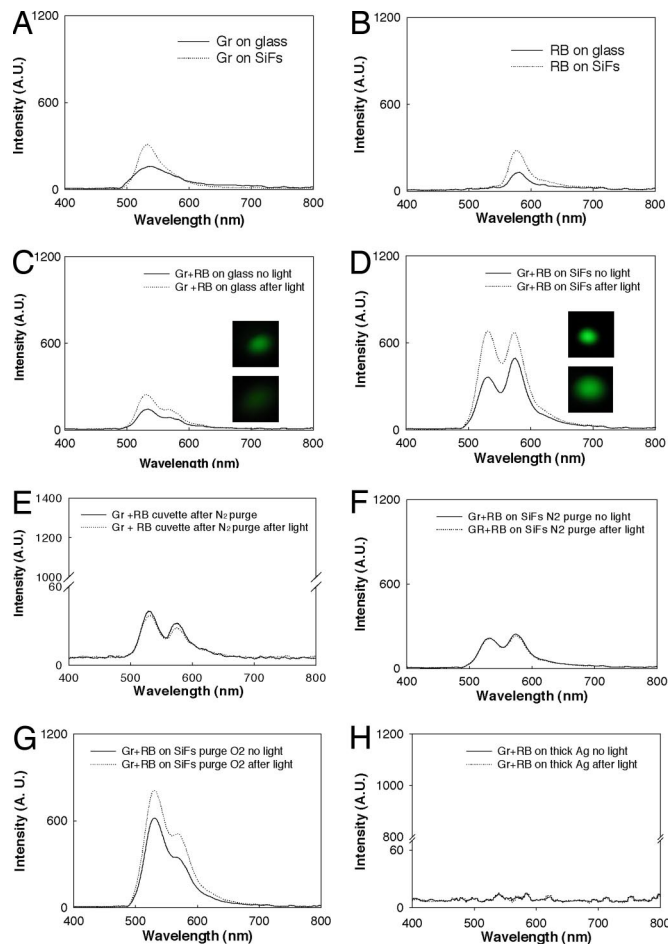


Fig. 2. Metal-enhanced singlet oxygen generation studies. Shown are fluorescence emission spectra of green sensor (Gr) (A), RB (B), and a mixture of both on glass (C), SiFs (D), in cuvette (E), on SiFs nitrogen purged (F), on SiFs oxygen purged (G), and on 50 nm thick Ag (H), before and after light exposure (2 min) at room temperature. The light source was a 100-W mercury lamp. $\lambda_{\text{ex}} = 473\text{ nm}$.

sure to UV light, reflecting an increase in singlet oxygen yield. On SiFs (Fig. 2D *Insets*), this increased brightness of the solution is more pronounced, further suggesting that the presence of the Ag nanoparticles facilitates increased singlet oxygen generation consistent with a previous report from our laboratory (13).

Because we compare SiFs to a glass substrate for the production of enhanced singlet oxygen generation, it is important to discuss the similarities in the surface features of these substrate materials. As described in the previously published procedure (10), SiFs are deposited onto the same glass substrate (used for the comparison of singlet oxygen generation) as particles with a diameter on the order of 100 nm and a surface coverage of $\approx 40\%$. Thus, the comparison of a blank glass substrate with the same glass substrate containing SiFs for singlet oxygen generation is deemed appropriate.

To confirm that the observed signal enhancement in the presence of SiFs is due to an increase in singlet oxygen yield due to silver, we varied the oxygen supply. After extensively purging the RB and GR solution with N_2 and subsequent exposure to UV irradiation, we observed that the amplitude of the peak at 525 nm did not change in the cuvette (Fig. 2E) or on SiFs (Fig. 2F). As expected, these results indicate that no singlet oxygen was generated. However, after purging the

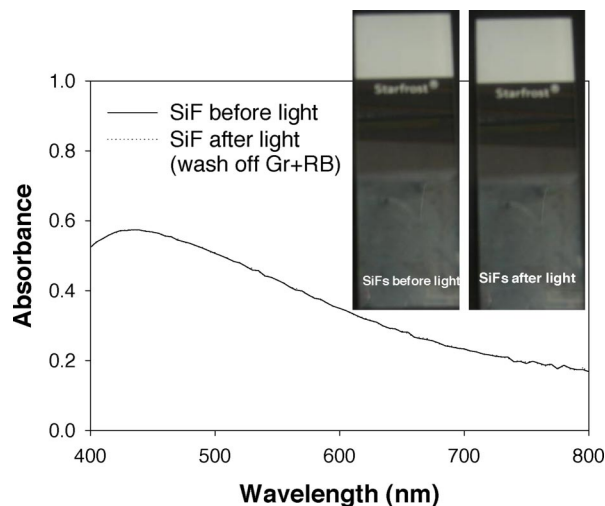


Fig. 3. Absorption spectroscopy studies. Shown are absorption spectra of SiFs before and after light, showing no effect on the silvered surface by $^1\text{O}_2$ (light-UV exposure).

mixture of RB and GR solution with oxygen and subsequent exposure to UV irradiation (sensitization), we observe a sharp increase in the GR fluorescence peak intensity from SiFs due to singlet oxygen generation (Fig. 2G). A mixture of RB and GR solution on a continuous silver strip was also studied (Fig. 2H) because surface plasmons cannot be generated in a continuous strip of metal (from the air side) but of course can be in noncontinuous particulate SiFs. No enhanced singlet oxygen generation was observed on the continuous silver strip, giving further evidence for our plasmon-enhanced triplet yield mechanism.

To demonstrate that the SiFs are unaffected by $^1\text{O}_2$ or UV irradiation, we compared the absorption spectra of SiFs before UV irradiation and SiFs previously coated with the GR/RB mixture and exposed to UV irradiation (Fig. 3). We observed no change to the plasmon absorbance spectra for the SiFs samples before and after UV irradiation. Subsequently, we concluded that there were no structural changes to the SiFs or surface plasmon oscillation, which could otherwise account for our observations.

To demonstrate that our approach for enhancing triplet yields is not limited to solutions of RB, we also tested the enhancement of singlet oxygen yield for many other photosensitizers with singlet oxygen quantum yields varying from 0.08 to 1.00 (Fig. 4). To calculate the singlet oxygen enhancement of these photosensitizers, we first calculated the MEF factor of the photosensitizer GR [MEF from green photosensitizer before exposure to UV light (Fig. 2A)]. The MEF factor of the photosensitizer, $GR_{\text{MEF,before}}$, on SiFs is calculated by

$$GR_{\text{MEF,before}} = \frac{\int_0^\infty GR_{\text{SiF,before}} d\lambda}{\int_0^\infty GR_{\text{GL,before}} d\lambda}, \quad [1]$$

where $\int_0^\infty GR_{\text{SiF,before}} d\lambda$ and $\int_0^\infty GR_{\text{GL,before}} d\lambda$ are the integrated spectra (Fig. 2C) for the green sensor dye (GR), before exposure to UV light on SiFs and glass substrates (GL), respectively. The calculation of the MEO (metal-enhanced singlet oxygen yield) of the photosensitizer is as follows:

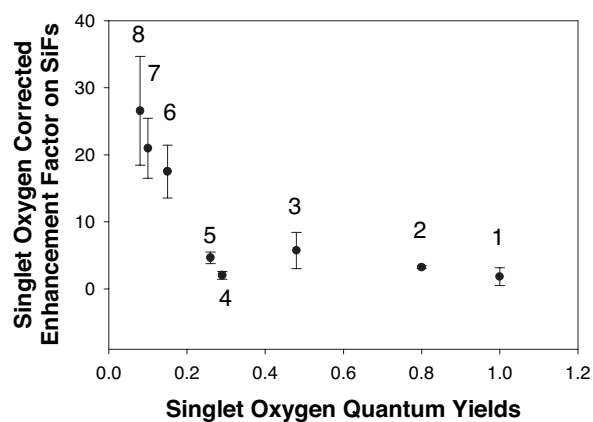


Fig. 4. Singlet oxygen enhancement factor for a variety of photosensitizers. Shown is the singlet oxygen corrected enhancement factor on SiFs versus free-space singlet oxygen quantum yield. 1, acridine; 2, RB; 3, chloroquine; 4, indomethacin; 5, riboflavin; 6, naproxen; 7, chlorpromazine; 8, quinidine. Error bars are based on the standard deviation of three spectral measurements.

$$^1\text{O}_{2,\text{MEO}} = \frac{\int_0^\infty (GR, RB)_{\text{SiF,after}} d\lambda - \int_0^\infty RB_{\lambda_n, \text{SiF,after}} d\lambda}{GR_{\text{MEF,before}} \left(\int_0^\infty (GR, RB)_{\text{GL,after}} d\lambda - \int_0^\infty RB_{\text{GL,after}} d\lambda \right)}, \quad [2]$$

where $\int_0^\infty RB_{\text{SiF,after}} d\lambda$, $\int_0^\infty RB_{\text{GL,after}} d\lambda$, $\int_0^\infty (GR, RB)_{\text{SiF,after}} d\lambda$, and $\int_0^\infty (GR, RB)_{\text{GL,after}} d\lambda$ are the integrated spectra for RB and the mixture of photosensitizer (GR) with RB after exposure to UV light on SiFs and glass substrates (GL), respectively (Fig. 2D). The enhancement factor is 26.6 ± 8.13 for quinidine, which has a free-space singlet oxygen quantum yield of 0.08. In contrast, for acridine, which has a high singlet oxygen yield of 1.00, the enhancement factor is 1.83 ± 1.35 . Interestingly, the enhanced singlet oxygen yield factor appears to be inversely proportional to free-space singlet oxygen yield. This finding is consistent with the MEF enhancement factor for fluorophores and (relative intensities in the presence and absence of metal for the fluorophores) increases as the free-space quantum yield (Q_0) decreases (26).

To determine the distance dependence of ME^1O_2 , SiO_x layers of 0.5, 2, 5, and 10 nm thickness were vapor-deposited on SiFs (Fig. 5D). We observed that the amplitude of the emission spectra of GR and RB solution on SiFs varied with different thickness of SiO_x (Fig. 5C). The singlet oxygen enhancement factor of GR and RB solution on SiFs was 2.0-fold for 0.5-nm SiO_x coatings, 1.5-fold for 2.0-nm SiO_x , 1.3-fold for 5-nm SiO_x coatings, and no enhancement for 10-nm SiO_x (Fig. 5C). These values and distances are again consistent with the enhanced absorption effect (enhanced electric field), which partially contributes to the enhanced intensities observed in MEF (27).

To subsequently correlate the electric field enhancements of the incident excitation radiation on the SiFs (28) with the distance dependence of the RB photosensitizer from the metal, we used FDTD calculations to simulate the electric field enhancements of a 365-nm source around a 100-nm silver nanoparticle (Fig. 5A and B). This size is equivalent to the average particle size for SiFs used in these experiments (29). We observed that a nonlinear relationship exists between the experimentally calculated distance-dependent enhancement of

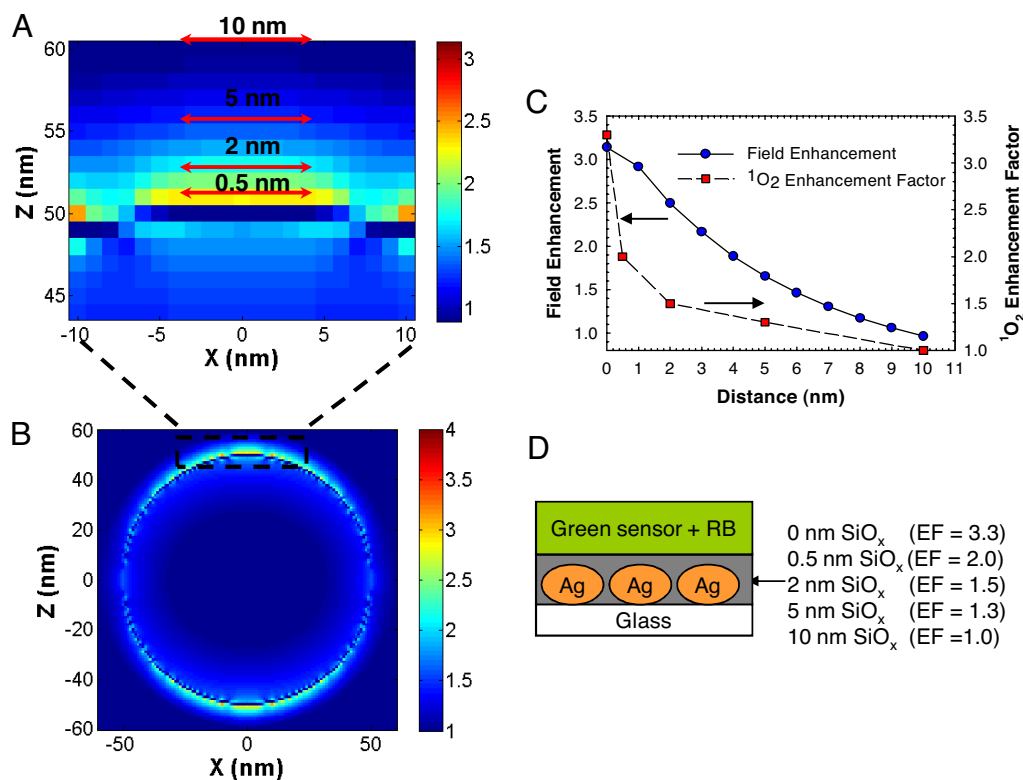


Fig. 5. FDTD calculations for field enhancements around a silver sphere. (A) Zoomed image of 10 nm above the surface of the silver sphere maximum field intensity at $z = 10$ nm to correlate increased field enhancements in proximity to sphere surface with increased singlet oxygen generation. (B) $|E|^2$ field intensity (incident plus scatter) distribution in the xz plane around a 100-nm silver sphere due to an incident TFSF wave propagating along the y axis and polarized along the z axis with a wavelength of 365 nm, which corresponds to the maximum wavelength of the UV source used to excite RB and generate singlet oxygen. (C) Distance dependence relationship between electric field enhancements and singlet oxygen on 100-nm Ag nanoparticles. (D) Distance dependence of singlet oxygen enhancement factor of RB on SiFs. The top layer is mixed solution of green sensor and RB. The SiO_x layer was deposited by using thermal vapor deposition. Ag, silver island films; EF, enhancement factor.

singlet oxygen yields for SiO_x films deposited on SiFs and the simulated electric field enhancements (Fig. 5C).

In our previous studies, we demonstrated that the enhanced fluorescence, or MEF, is a result of both a net system absorption and plasmon coupling and efficient emission, but we have been unable to quantify the relative contributions of enhanced emission and net increase in the system absorption to the MEF phenomena (12). Due to the increase in the population of the singlet excited state or net system absorption, we have also presented evidence for a subsequent increase in the population of the triplet state for RB (12). To confirm this result, we demonstrated MEP at low temperature (12). Previously, we described a net increase in the system absorption for RB as contributing in part to both MEF and MEP at low temperature (12). We do not observe the phosphorescence emission at room temperature even though the plasmon-coupling and emission is a fast process (25). The rate of quenching of excited triplet states is greater than the rates of back intersystem crossing and phosphorescence emission (25). Because spin orbit coupling for RB in the presence SiFs is also negligible (12) (Fig. 2H), we also ignore the relaxation rate of the excited triplet state to the ground state, S₀. In addition, we note that there is no observed triplet-triplet absorption at room temperature (25).

Subsequently, we suggest that the enhanced singlet oxygen yields for photosensitizers in proximity to a metal nanoparticle are a function of the net system absorption, which can be theoretically calculated by using FDTD calculations. In addition, we believe that our approach also has provided a framework to experimentally quantify the contribution of increased system

absorption and MEF. This observation is helpful not only in creating surface architectures for optimizing singlet oxygen generation, but also in our laboratory's continued efforts to develop a unified plasmon-fluorophore description (27).

Conclusions

In this article, we have reported the observation of plasmon-enhanced ¹O₂ generation and parameters for optimizing ¹O₂ generation based on the distance dependence of a sensitizer to metallic nanoparticles. Our findings suggest that an increase in the net system absorption facilitates metal-enhanced singlet oxygen and MEF at room temperature. Using electromagnetic field calculations to predict electric field distributions, we believe that the extent of enhanced triplet yields and the subsequent rates of singlet oxygen production of luminophores/fluorophores in close proximity to plasmonic structures can be readily predicted. Recently, we reported the solution-based embodiment of MEF in a nanoball architecture (30). These particles were constructed with solid metallic cores with an outer SiO₂ coating. Both the core diameter and shell thickness can be varied for optimum MEF and can accommodate virtually any fluorophore/luminophore, potentially allowing photosensitizers also to be incorporated within the shells for singlet oxygen generation. Given that the nanoballs are small enough for cellular entry and vascular diffusion, they are potentially valuable for PDT. The combination of nanoparticles with singlet oxygen generation may generate a new research field with wide ranging applications, especially in PDT.

Materials and Methods

Silver nitrate (99.9%), sodium hydroxide (99.996%), ammonium hydroxide (30%), D-glucose, and premium quality silane-prep glass slides (75 × 25 mm) were obtained from Sigma. The singlet oxygen green sensor reagent (GR) was obtained from Molecular Probes/Invitrogen and is highly selective for $^1\text{O}_2$. In the presence of singlet oxygen, it emits a green fluorescence (excitation/emission 504/525 nm) (24). RB, acridine, chloroquine, indomethacin, riboflavin, naproxen, and chlorpromazine quinidine were also obtained from Sigma. All chemicals were used as received.

Preparation of SiFs. SiFs were prepared according to ref. 29.

Preparation of Sandwich Format Samples. A solution of 500 μl of photosensitizer (0.1 mM) in water and 500 μl of GR (4.5 mM) (also in water) was sandwiched between glass slides and SiFs, respectively. The glass/SiF surfaces were exposed to a mercury lamp (UV-light, 365 nm, 100 W) for 2 min for singlet oxygen generation and also used for the post-UV-irradiation measurements.

Absorption and Fluorescence Measurements. Absorbance spectra were taken by using a Varian Cary 50 UV-vis spectrophotometer. Fluorescence emission was collected at 45° to the excitation through a long-pass filter, using a fiber optic spectrometer from Ocean Optics (HD2000). A 473-nm laser line was used for excitation.

Singlet Oxygen Yield Enhancement Factor Measurements. On SiFs, the enhancement factor was calculated from

$$GR_{\text{MEF,before}} = \frac{\int_0^\infty GR_{\text{SiF,before}} d\lambda}{\int_0^\infty GR_{\text{GL,before}} d\lambda}, \quad [3]$$

where $\int_0^\infty GR_{\text{SiF,before}} d\lambda$ and $\int_0^\infty GR_{\text{GL,before}} d\lambda$ are the integrated spectra (Fig. 2A) for the green photosensitizer (GR), before exposure to UV light on SiFs and

glass substrates (GL), respectively. The calculation of the MEO (metal-enhanced singlet oxygen yield) of the photosensitizer is as follows

$$^1\text{O}_{2,\text{MEO}} = \frac{\int_0^\infty (GR, RB)_{\text{SiF,after}} d\lambda - \int_0^\infty RB_{\lambda_n, \text{SiF,after}} d\lambda}{GR_{\text{MEF,before}} \left(\int_0^\infty (GR, RB)_{\text{GL,after}} d\lambda - \int_0^\infty RB_{\text{GL,after}} d\lambda \right)},$$

where $\int_0^\infty RB_{\text{SiF,after}} d\lambda$, $\int_0^\infty RB_{\text{GL,after}} d\lambda$, $\int_0^\infty (GR, RB)_{\text{SiF,after}} d\lambda$, and $\int_0^\infty (GR, RB)_{\text{GL,after}} d\lambda$ are the integrated spectra for RB and the mixture of photosensitizer (GR) with RB after exposure to UV light on SiFs and glass substrates (GL), respectively.

FDTD Simulations. The FDTD method was used here to determine the electric field intensities and distributions at the surface of a 100-nm silver nanoparticle in a total field scattered field. These results were compared with Mie theory and previously published reports to verify the accuracy of the model (18). Total-field scattered-field sources are used to divide the computation area or volume into total-field- (incident plus scattered field) and scattered-field-only regions (31). The incident field is defined as a plane wave with a wavevector that is normal to the injection surface and the scattered and total field are monitored during the simulation such that the total or scattered transmission can be measured. By using Lumerical FDTD Solution software, the simulation region was set to $700 \times 700 \times 700 \text{ nm}^3$ with a mesh accuracy of 6. To minimize simulation times and maximize the resolution of field enhancement regions around the metal sphere, a mesh override region was set to 1 nm around the 100-nm Ag sphere. The overall simulation time was set to 200 ns and calculated over a frequency range of 300 to 600 nm, where a plasma model was used to represent the properties of the silver nanoparticle in the range of 300 to 600 nm.

ACKNOWLEDGMENTS. We thank the University of Maryland Biotechnology Institute, the Medical Biotechnology Center, and the Institute of Fluorescence for support.

- Demidova TN, Hamblin MR (2004) *Int J Immunopathol Pharmacol* 17:245–254.
- Brown SB, Brown EA, Walker I (2004) *Lancet Oncol* 5:497–508.
- Kendall CA, Morton CA (2003) *Technol Cancer Res Treat* 2:283–288.
- Dougherty TJ (2002) *J Clin Laser Med Surg* 20:3–7.
- Jarvi MT, Niedre MJ, Patterson MS, Wilson BC (2006) *Photochem Photobiol* 82:1198–1210.
- Moan J, Peng Q, Sorensen R, Iani V, Nesland JM (1998) *Endoscopy* 30:387–391.
- Bauer J, Chen KH, Hiltbunner A, Wehrli E, Eugster M, Schnell D, Kessler F (2000) *Nature* 403:203–207.
- Thompson MS, Johansson A, Johansson T, Andersson-Engels S, Svanberg S, Bendsoe N, Svanberg K (2005) *Appl Opt* 44:4023–4031.
- Geddes CD, Lakowicz JR (2002) *J Fluoresc* 12:121–129.
- Aslan K, Leonenko Z, Lakowicz JR, Geddes CD (2005) *J Fluoresc* 15:643–654.
- Zhang Y, Aslan K, Malyn SN, Geddes CD (2006) *Chem Phys Lett* 427:432–437.
- Zhang Y, Aslan K, Previte MJR, Malyn SN, Geddes CD (2006) *J Phys Chem B* 110:25108–25114.
- Zhang YX, Aslan K, Previte MJR, Geddes CD (2007) *J Fluoresc* 17:345–349.
- Barber PW, Chang RK, Massoudi H (1983) *Phys Rev B* 27:7251–7261.
- Yang WH, Schatz GC, Vanduyne RP (1995) *J Chem Phys* 103:869–875.
- Yee KS, Chen JS (1997) *IEEE Trans Antennas Propag* 45:921–925.
- Kelly KL, Coronado E, Zhao LL, Schatz GC (2003) *J Phys Chem B* 107:668–677.
- Challener WA, Sendur IK, Peng C (2003) *Opt Express* 11:3160–3170.
- Yee KS (1966) *IEEE Trans Antennas Propag* 14:302–307.
- Foteinopoulou S, Vigneron JP, Vandenbem C (2007) *Opt Express* 15:4253–4267.
- Hao E, Schatz GC (2004) *J Chem Phys* 120:357–366.
- Redmond RW, Gamlin JN (1999) *Photochem Photobiol* 70:391–475.
- Hideg E, Barta C, Kalai T, Vass I, Hideg K, Asada K (2002) *Plant Cell Physiol* 43:1154–1164.
- Flors C, Fryer MJ, Waring J, Reeder B, Bechtold U, Mullineaux PM, Nonell S, Wilson MT, Baker NR (2006) *J Exp Bot* 57:1725–1734.
- Stiel H, Teuchner K, Paul A, Leupold D, Kochevar IE (1996) *J Photochem Photobiol B* 33:245–254.
- Lakowicz JR (1999) *Principles of Fluorescence Spectroscopy* (Kluwer Academic, New York).
- Aslan K, Previte MJR, Zhang YX, Geddes CD (2007) *Biophys J* 371A (abstr).
- Xu HX, Wang XH, Persson MP, Xu HQ, Kall M, Johansson P (2004) *Phys Rev Lett* 93:243002.
- Aslan K, Gryczynski I, Malicka J, Matveeva E, Lakowicz JR, Geddes CD (2005) *Curr Opin Biotechnol* 16:55–62.
- Aslan K, Wu M, Lakowicz JR, Geddes CD (2007) *J Am Chem Soc* 129:1524–1525.
- Anantha V, Taflove A (2002) *IEEE Trans Antennas Propag* 50:1337–1349.